

RESEARCH ARTICLE | JUNE 14 2024

Dual-function optical modulation and detection in microring resonators integrated graphene/MoTe₂ heterojunction **FREE**

Jianghong Wu ; Jialing Jian ; Boshu Sun ; Yuting Ye ; Hui Ma ; Bo Tang ; Qingyan Deng ; Renjie Tang ; Junying Li ; Chunlei Sun ; Hongtao Lin ; Lan Li  

 Check for updates

Appl. Phys. Rev. 11, 021426 (2024)

<https://doi.org/10.1063/5.0207874>



View
Online



Export
Citation



APL Quantum
First Articles Online
No Article Processing Charges for Submissions
Through December 31, 2024
[Read Now](#)



Dual-function optical modulation and detection in microring resonators integrated graphene/MoTe₂ heterojunction

Cite as: Appl. Phys. Rev. **11**, 021426 (2024); doi: [10.1063/5.0207874](https://doi.org/10.1063/5.0207874)

Submitted: 12 March 2024 · Accepted: 27 May 2024 ·

Published Online: 14 June 2024



View Online



Export Citation



CrossMark

Jianghong Wu,^{1,2,3}  Jialing Jian,^{1,2}  Boshu Sun,^{1,2}  Yuting Ye,^{1,2}  Hui Ma,⁴  Bo Tang,⁵  Qingyan Deng,^{1,2} 
Renjie Tang,^{1,2}  Junying Li,⁴  Chunlei Sun,^{1,2}  Hongtao Lin,⁴  and Lan Li^{1,2,6,a)} 

AFFILIATIONS

¹Key Laboratory of 3D Micro/Nano Fabrication and Characterization of Zhejiang Province, School of Engineering, Westlake University, Hangzhou 310030, China

²Institute of Advanced Technology, Westlake Institute for Advanced Study, Hangzhou 310024, China

³Department of Applied Physics, The Hong Kong Polytechnic University, Hong Kong 999077, China

⁴State Key Laboratory of Modern Optical Instrumentation, College of Information Science and Electronic Engineering, Zhejiang University, Hangzhou 310027, China

⁵Institute of Microelectronics, Chinese Academic Society, Beijing 100029, China

⁶Westlake Institute for Optoelectronics, Fuyang, Hangzhou 311421, China

^{a)} Author to whom correspondence should be addressed: lilan@westlake.edu.cn

ABSTRACT

On-chip photonic devices such as modulators and photodetectors are essential building blocks for integrated photonics, enabling a wide range of applications in optical communication, sensing, and other emerging fields. Generally, optical modulation and photodetection are accomplished by two discrete devices in integrated photonic circuits, prohibiting the expansion of device functionality and the miniaturization of photonic systems. In this work, we demonstrate graphene/MoTe₂ heterojunction integrating with microring resonators (MRRs) to serve as an optical modulator under positive bias voltage and a photodetector under negative bias voltage at the telecom band. Such a device primarily benefits from graphene's optoelectronic characteristics, including broadband absorption and electrostatically tunable refractive index. The obtained dual-functional MoTe₂/graphene heterojunction devices demonstrate a modulation depth of ~26.7 dB, a bandwidth of 7.0 GHz, and a self-driven, wavelength-sensitive optoelectronic response at the telecom C band. Our studies indicate that combining graphene van der Waals heterojunction with MRRs paves the way to emerging photonic applications such as neuromorphic computing while expanding the freedom for miniaturized photonic circuits.

Published under an exclusive license by AIP Publishing. <https://doi.org/10.1063/5.0207874>

I. INTRODUCTION

Integrated photonics based on diverse photonic platforms such as silicon,¹ lithium niobate,² silicon nitride,³ and amorphous glass⁴ has drawn considerable attention because of widespread applications in optical communication,⁵ sensing technology,⁶ and computation.⁷ With the tremendous strides in integrated photonics, there is a mounting interest in developing a device architecture that offers multiple functions for space efficiency and improves system reliability and flexibility, thus providing new opportunities for emerging photonic schemes with potential massive impact.⁸ For instance, an on-chip one-unit photonic device with dual functions can serve as nonlinear

activation functions for neural networks^{9,10} and allow the reconfigurable operation for neuromorphic computing with substantially reduced power consumption.¹¹ However, a majority of these photonic platforms possess enormous obstacles for realizing one-unit devices with dual functions based on bulk semiconductors because epitaxial growth and heterogeneous integration are stringently limited by lattice mismatching and technical incompatibility. In contrast, two-dimensional materials (2DMs) can be compatible with arbitrary photonic platforms by van der Waals force, excluding the integration barriers induced by the variation of lattice constants and thermal expansion coefficients.

In the past decade, 2DMs with unique characteristics such as naturally terminated surface, broadband absorption, and tunable optoelectronic properties have already shown their advantages for integrated photonics.^{12–15} Among different 2DMs, graphene with electrostatically tuned optoelectronic behaviors is a typical material for on-chip photonic applications.^{16–18} However, most of the reported waveguide-integrated graphene photodetectors and modulators are based on two discrete units in prior research, which is limited by different device platforms for electron-to-photon and photon-to-electron transition. Generally, a graphene capacitor that induces charge concentration variation is naturally regarded as an effective structure for optical modulators, but it is invalid for photodetectors because of the bottleneck of carrier migration and collection.¹⁹ In contrast, the generation–separation–collection processes of photoinduced carriers in the metal–graphene–metal structure are essential for a photodetector, but it is ambitious to produce the optical characteristics variation for achieving efficient optical modulation.¹⁹ Therefore, developing a simplified structure design for the one-unit device with dual modulator and photodetector functionalities remains enormously attractive.

In this paper, we combined a graphene/MoTe₂ heterojunction with a micro-ring resonator (MRR) to demonstrate a single device that can simultaneously function as an optical modulator and a photodetector. In such a compact device, monolayer graphene works as the primary photoactive material, which possesses both the tunable refractive index for modulation and the ability of photon-to-electron transition for photodetection. Concurrently, multilayer MoTe₂ (about 15 nm thick) with negligible optical absorption at the C band plays a significant role in regulating optical parameters of the bottom graphene. Moreover, an MRR that facilitates photon circulation in the cavity can effectively enhance light–matter interaction and optimize device performance. As a result, we realized both an optical modulator and photodetector for the fundamental mode of TE polarization (TE₀) based on graphene/MoTe₂ heterojunction with a heterojunction length of less than 30 μm along the direction of an MRR. The compact device demonstrates the modulation depth and efficiency of 26.7 dB and 2.5 dB · V⁻¹, respectively, a f_{3dB} bandwidth of 7.0 GHz, and a self-driven, wavelength-sensitive optoelectronic response at the C band. The proposed heterojunction device with dual functions makes integrated photonic circuits more programmable and adaptable and brings about the possibility of more compact integrated photonic circuits.

II. RESULTS AND DISCUSSION

In order to implement the functionalities of both optical modulation and detection upon a single device, field effect transistor architectures in Figs. 1(a) and 1(b) are usually used to tune the refractive index for optical modulation by controlling carrier concentration with V_g and realize photon-to-electron transition for detection by collecting photo-induced carriers with V_d.^{20–22} However, this device architecture leads to an increased fabrication complexity and device performance degradation. As for optical devices based on a double-layer graphene capacitor in Fig. 1(a), dielectric deposition upon graphene is indispensable, but it is inevitably hindered by the chemically inert surface of graphene that makes nucleation and growth of a dense dielectric difficult.²³ Second, double-layer graphene brings about an undesirable optical insertion loss for the modulator.^{24,25} As for devices based on graphene–dielectric–silicon capacitors in Fig. 1(b), the separate doping processes for silicon ridge waveguides are essential, introducing both the fabrication complexity and the optical loss due to free carrier

absorption (usually several decibel per millimeter).²⁶ Meanwhile, the implementation of the graphene–dielectric–ridge waveguide capacitor architecture in alternative integrated photonic platforms, such as SiNx and polymer, poses challenges due to the complexity of accomplishing the doping requirement for back-gate electrode construction. Additionally, photodetectors based on metal–graphene–metal suffer from a large dark current and shot noise. In contrast, graphene heterojunction in Fig. 1(c) expands the operation flexibility for realizing both modulators and photodetectors and simplifies the fabrication procedures, where both electron-to-photon and photon-to-electron transition can be realized by applying a suitable V_d. In such a heterojunction, 2D semiconductors with a bandgap larger than the photon energy at the telecom C-band are suitable for minimizing insertion loss. Multilayer MoTe₂ is particularly advantageous in such a device architecture, as it possesses small optical absorption at the telecom C-band, making it a promising candidate for optical devices with large bandwidth.^{27,28}

A typical graphene heterojunction optical device with dual function is configured as the MoTe₂–graphene–SiO₂–Si waveguide structure in Fig. 1(c), where a monolayer graphene works as a photoactive material whose optical characteristics can be electrostatically tuned with the accumulation and depletion of free electron. Simultaneously, photon-to-electron transition at a broadband wavelength range can be realized by monolayer graphene due to the semi-metal property. The middle SiO₂ (~15 nm-thick) is used to construct a flat surface, protecting graphene from fracturing. In this device, the junction region of graphene/MoTe₂ heterostructure is primarily located upon the optical waveguide, as shown in Fig. 1, which is verified by a typical scanning electron microscope (SEM) image in Fig. 1(e). During the fabrication, we transferred monolayer graphene before depositing metal pads (Ti/Au: 5/100 nm) and subsequently transferred MoTe₂ (the detailed device fabrication processes shown in Fig. S1) to connect graphene with another metal pad, which reduces the complexity of the device fabrication but leads to large contact resistance between MoTe₂ and metal pad as well.²⁹

We then collected their Raman spectra to verify material's quality in Fig. 2(a), and the characteristic peaks of a bare MoTe₂ flake indicate that it is the hexagonal phase. Simultaneously, the graphene flake shows two primary Raman peaks at 1590 (G mode) and 2682 (2D mode) cm⁻¹, and the ratio of peak intensity (I_{2D}/I_G) indicates that graphene is monolayer and slightly doped.³⁰ Meanwhile, the defect peak (D mode) is extremely weak, confirming the limited defects on the graphene sheet. As for the Raman peak of the graphene sheet under a MoTe₂ flake, the red shift of G mode and the reduction of I_{2D}/I_G ratio indicate changes in the doping level of graphene resulting from carrier transfer at the interface of graphene/MoTe₂ heterojunction.³¹ The carrier transfer at the junction is primarily driven by the work function difference, verified by the Kelvin probe force microscope (KPFM) characterization. The measured contact potential difference for a graphene/MoTe₂ heterojunction indicates that MoTe₂ (30 nm-thick) possesses a larger surface potential than that of graphene in Fig. 2(b), and the work function difference between graphene and MoTe₂ is about 153 meV (Fig. S2), leading to electron transfer from MoTe₂ to graphene at the interface. Additionally, multi-layer MoTe₂ flakes show weak photoluminescence as a result of an indirect bandgap at telecom O bands (Fig. S2).

The changes in graphene's Fermi level can be realized by controlling the applied bias voltages upon the graphene/MoTe₂ heterojunction

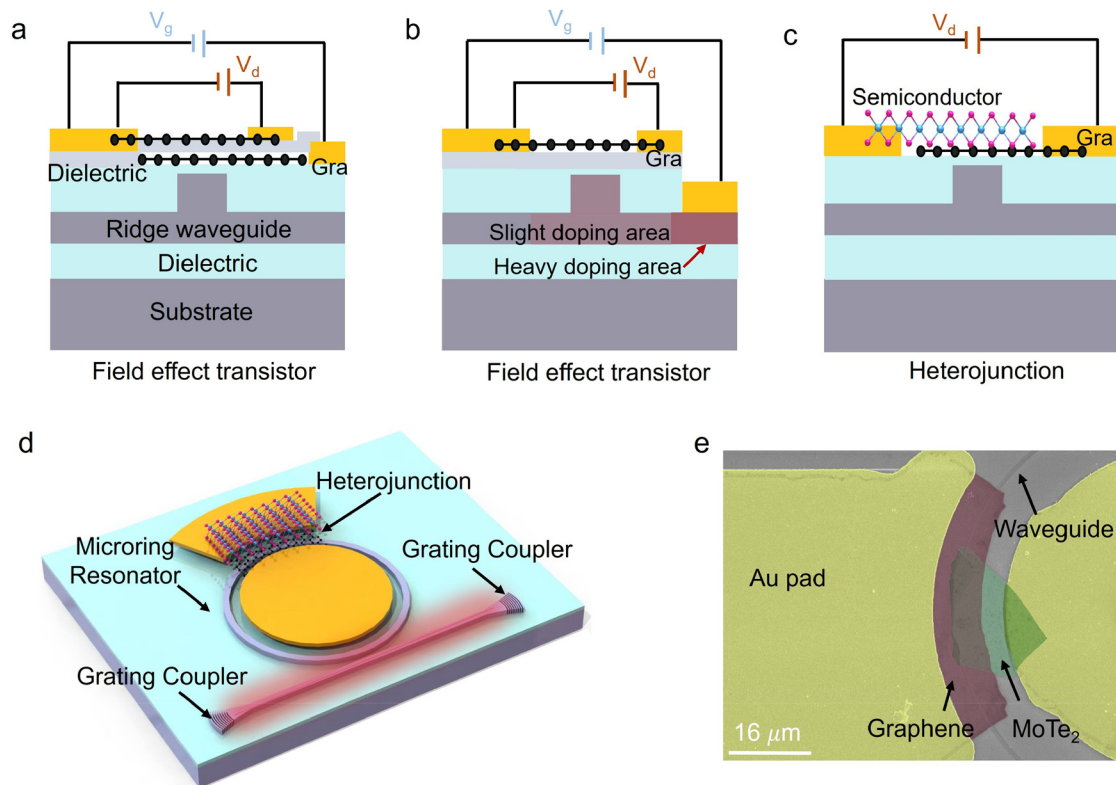


FIG. 1. Dual-function device architectures for optical modulation and photodetection based on graphene field effect transistor, where another monolayer graphene (a) and rigid waveguide (b) serve as back-gate electrodes. Optical modulation and detection can be realized by applying suitable V_g and V_d , respectively. (c) Waveguide-integrated dual-function devices based on graphene heterojunction. (d) Schematic diagram of graphene/MoTe₂ heterojunction device integrating with an MRR, light is guided in/out by two opposite grating couplers, and the overlapping junction region is located upon an MRR. (e) A false-color SEM image of an MRR-integrated graphene/MoTe₂ heterojunction device.

as shown in the energy band structure in Figs. 2(c)–2(e), which thus can bring about the variation of optical absorption and refractive index. Chemical vapor deposition-grown (CVD-grown) monolayer graphene after the wet transfer is slightly p-doped³² and multilayer MoTe₂ is p-doped because of the “on” state located at a negative gate voltage (Fig. S3). At equilibrium, electrons transfer from MoTe₂ to monolayer graphene, complying with the work function difference in Fig. 2(b), and the Fermi level of graphene at 0 V is below the Dirac point, inferred from monotonical change in extinction ratio under different bias voltages [Figs. 3(b) and S4]. Notably, MoTe₂ thickness is less than 40 nm in our devices; therefore, it is fully depleted. Under a positive bias voltage, the length of the depletion layer (primarily in MoTe₂) is shortened, and even more holes are accumulated in graphene in Fig. 2(d). In contrast, many more electrons are accumulated in monolayer graphene under a reverse bias voltage in Fig. 2(e), bringing about the Fermi level being close to and even higher than the Dirac point, which is consistent with the MRR transmission spectra [Fig. S4(b)]. The Fermi level variation effectively tunes the optical absorption, abiding by the Pauli blocking effect.³³ Specifically, incident light with photon energy being larger than $2|\mu|$ (μ : chemical potential, $\mu=0$ represents the Fermi level located at the Dirac point) can be absorbed by graphene, and optical transparency undergoes a sharp increase for low-energy photons [Fig. S5a(i)].

Moreover, optical absorption can also be regulated by the density of free carriers in the “conduction band,” and a smaller occupation can bring a larger optical absorption (Fig. S5a(ii) and S5a(iii)). Therefore, the optical absorption of graphene in such a graphene/MoTe₂ heterojunction device can be evidently tuned by external bias voltage.

Graphene possesses a larger tunable optical absorption when the Fermi level is below the Dirac point;³⁴ therefore, a graphene/MoTe₂ heterojunction optical modulator works efficiently under a positive bias voltage. Concurrently, MRRs are designed to enhance light–matter interaction, and the operational principle for picking up MRRs is discussed (Fig. S6). Taking an MRR (300 nm gap) as an example for elucidating the operational principle, graphene at the initial condition (0 V) with the Fermi level being close to the Dirac point induces a large optical loss, preventing photon circulation in the cavity; thus, the majority of incident light would pass through the bus waveguide in Fig. 3(a). In contrast, the decrescent optical loss in the cavity under a positive bias voltage, as a result of the Fermi level being farther away from the Dirac point, makes the MRR change gradually from the under-coupled to the critically coupled condition in Fig. 3(a), resulting in the optical energy at resonance wavelengths being trapped in the cavity. Such a tunable optical loss in the cavity is significant for optical modulators and switches.

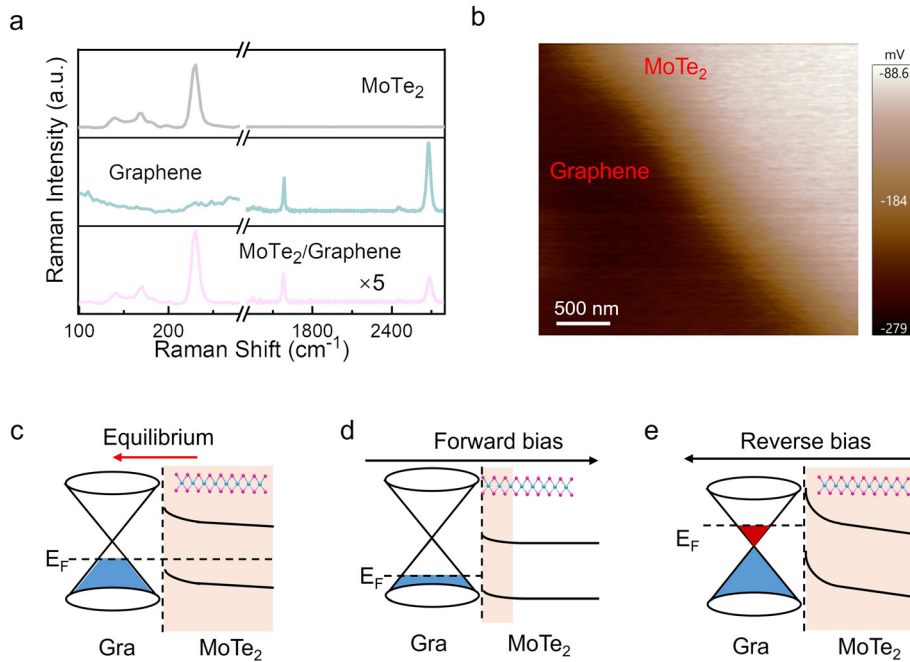


FIG. 2. Characterization of graphene/MoTe₂ heterojunction. (a) Raman spectra of bare graphene, graphene under MoTe₂ (heterojunction region), and bare MoTe₂ under the excitation of a 532-nm laser. (b) Surface potential image of the graphene/MoTe₂ heterojunction measured by KPFM. (c) At equilibrium, electrons diffuse from MoTe₂ to graphene, leading to a depletion layer, and MoTe₂ is fully depleted because of its thin thickness in the proposed device. The orange, blue, and red regions and red arrows represent the depletion region, the energy level occupied with bound and free electrons, and the direction of the built-in field, respectively. (d) Under a positive bias voltage, holes are accumulated upon graphene with the contraction of the depletion region length. (e) Under a reverse bias voltage, electrons are accumulated onto graphene.

The transmission spectra of an MRR integrating with graphene/MoTe₂ heterojunction under different bias voltages in Fig. 3(b) indicate that optical modulation can be realized. Initially, the ER of an undercoupled MRR is about 7 dB at the wavelength of ~ 1546 nm. With the applied bias voltage increment, this MRR becomes progressively more critically coupled, resulting in the gradually improved ER with a maximum of about 32 dB in Fig. 3(b). Simultaneously, the transmission dip reaches a saturation point, indicating that the graphene fully enters the Pauli blocking region and then the tunable electro-refractive response becomes the primary principle for optical phase modulation under the larger bias voltages.³⁵ Therefore, the blue shift of resonance peak on the wavelength axis is then observed, which is mostly attributed to the non-monotonic gate-dependent electro-refractive response of graphene.³⁶

To analyze the ER variation and resonance wavelength shift, the effective refractive index [$\text{Im}(n_{\text{eff}})$] of Si/graphene/MoTe₂ hybrid waveguide at 1550 nm has been calculated, in which the refractive index of graphene as a function of chemical potential has been obtained previously.³⁷ As shown in Fig. 3(c), the calculated imaginary part of the $\text{Im}(n_{\text{eff}})$ of hybrid waveguide undergoes a slight change when the graphene chemical potential varies from 0 to 0.35 eV at the wavelength of 1550 nm, and it is reduced by ~ 20 times as the chemical potential changes from 0.35 to 0.48 eV, eventually approaching zero for the chemical potential exceeding 0.50 eV [Fig. 3(c)]. Intriguingly, such a multilayer hybrid waveguide shows a low mode mismatching loss for TE₀ [illustration in Fig. 3(c), MoTe₂ thickness: 15 nm], partially preventing the optical insertion loss. As for the real part of the effective refractive index, it is non-monotonic and the maximum value is located at the chemical potential of ~ 0.4 eV, which is consistent with the previous report.³⁸ As described, the ER, quality factor (Q) variation [Fig. S4(d)], and resonance wavelength shift are in good argument to

the theoretical analysis. Notably, optical parameters of MoTe₂ were regarded as the constant during the theoretical calculation, but the slight refractive index variation probably remains as a result of the plasma dispersion effect induced by the carrier concentration change in MoTe₂,^{39,40} which principally accounts for the ER and Q reduction at 16 V [Figs. S4(c) and S4(d)]. Furthermore, the static modulation depth (MD) can reach up to 25 dB at 10 V [Fig. S4(c)], which is even larger than previous graphene-based modulators,^{41,42} and can be predominantly attributed to three factors. First, an MRR brings about photon circulation in the cavity, thus enhancing the light-matter interaction. Second, a Si/graphene/MoTe₂ hybrid waveguide provides a larger optical field overlap with graphene than that in a Si/graphene hybrid waveguide (Fig. S7), producing a larger $\text{Im}(n_{\text{eff}})$ D-value. Within a certain thickness range, such a hybrid waveguide dramatically enhances the modulation efficiency [Fig. S7(a)], but the mode mismatching occurs when MoTe₂ is thicker than 60 nm [Fig. S7(c)]. Third, carrier concentration variation in graphene can be efficiently tuned by controlling the applied bias voltage in the heterojunction. To confirm the above-mentioned results for the modulator, graphene/MoTe₂ heterojunction was integrated with another MRR (Fig. S9), and similar optical loss and resonance peak wavelength shifts have been doubly confirmed.

We also measured the frequency response by an electrical vector network analyzer (VNA) (test setup shown in Fig. S10). The measured electro-optic bandwidth ($f_{3\text{dB}}$) bandwidth in Fig. 3(d) is about 7.0 GHz, where the thickness of the MoTe₂ flake is about 13 nm (Fig. S11). In the current stage, the maximum bandwidth is predominantly limited by RC time constant, especially, the large contact resistance between MoTe₂ and metal pads, and the large sheet resistance of MoTe₂. A higher bandwidth can be obtained by reducing the MoTe₂ length and optimizing contact resistance through the use of more

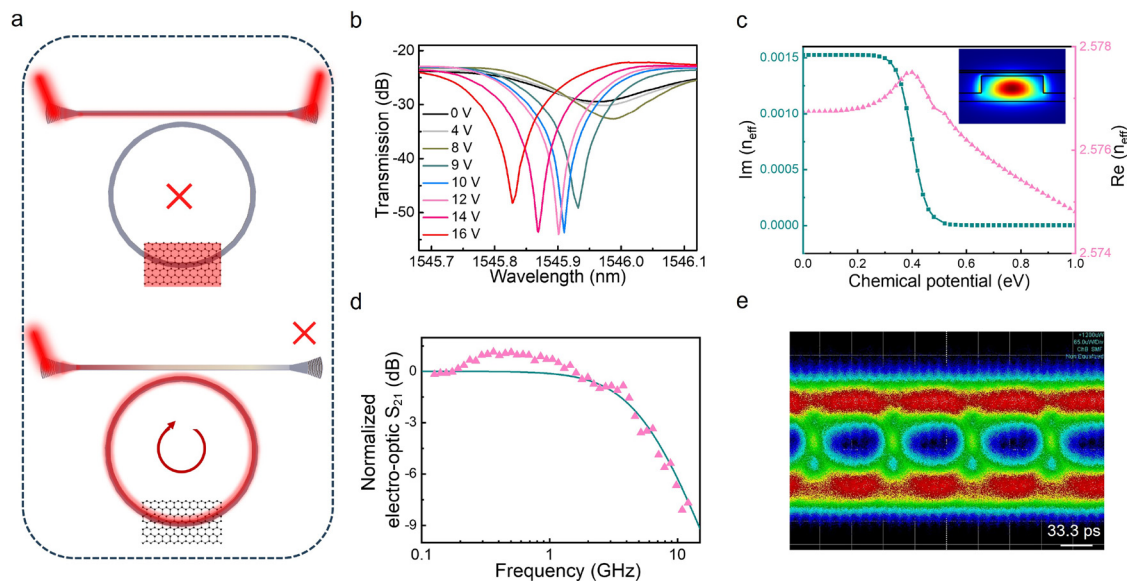


FIG. 3. Graphene/MoTe₂ heterojunction optical modulators. (a) Operational principle of graphene/MoTe₂ heterojunction integrated with an MRR. Graphene possesses large optical absorption in the initial condition, preventing light from circulating in the cavity. In contrast, optical absorption gradually diminishes under the positive bias voltage, resulting in light circulation in the cavity (spiral arrow). (b) Transmission spectra of an MRR integrating with the graphene/MoTe₂ heterojunction under different bias voltages. (c) Calculated effective refractive index of MoTe₂/graphene/Si hybrid waveguide of TE₀ mode as a function of chemical potential at 1550 nm. The illustration is the calculated optical mode in the hybrid waveguide (MoTe₂ thickness: 15 nm). (d) Electro-optic S_{21} bandwidth result, which is fitted by a single pole low-pass filter to extract the f_{3dB} . Line and triangle dots are fitting and experimental results. (e) Eye diagram characterization driven by the pseudo-random binary sequence. The device is biased at 10 V DC and driven with a 6.3 V peak-to-peak RF signal.

appropriate metals for Ohmic contact. Furthermore, to confirm the dynamic response, we characterized the optical response of an MRR modulator driven by a non-return-to-zero (NRZ) signal (test setup shown in Fig. S12) and observed an open 6 Gbps eye diagram in Fig. 3(e). The input signal is a $2^{31}-1$ pseudorandom binary sequence (PRBS) at 6.3 V peak to peak and under a 10.0 V DC bias voltage.

We then discuss the photon-to-electron transition at the C-band of the MRR-integrated graphene/MoTe₂ heterojunction devices. IV curves of a heterojunction device indicate that photon-to-electron transition at the C band can be realized, even without external bias voltage in Fig. 4(a). The Dark current of this heterojunction device is 0.3 nA at -1.0 V, and it increases to 65.4 nA (responsivity ~ 0.47 mA \cdot W⁻¹) with the optical excitation at 1550.78 nm. The small dark current can be primarily attributed to the large sheet resistance of multilayer MoTe₂ flake (Fig. S3) and depletion layer at the heterojunction interface. Moreover, the photocurrent excited by the resonance wavelength (1550.78 nm) is about sevenfold larger than that excited by the nonresonance wavelength (1550 nm) with the same input optical power. A flat multilayer MoTe₂ sheet possesses an optical bandgap larger than 1.0 eV, which is invalid for photon-to-electron transition at the C band.⁴³ The origin of photocurrent would be primarily attributed to the generation of hot electrons in graphene⁴⁴ and the collection of photoinduced carriers with the aid of an electric field in Fig. 4(b), which relies on the efficiency of both optical absorption and the carriers' separation-collection process. At 0 V, graphene possesses a large optical absorption, and the separation-collection process of electron-hole pairs can be realized by the built-in electric field; thereby, a self-driven photocurrent can be observed [Figs. 4(a) and 4(c)]. Under a reverse bias voltage, optical absorption would slightly decrease

according to transmission spectra [Fig. S4(b)], but the external electric field can promote the carriers' separation-collection process, resulting in a larger photocurrent. On the contrary, optical absorption weakens sensibly under the positive electric field; the electric field direction is opposite to that of the built-in electric field, hindering the carriers' collection and thus leading to a smaller photocurrent. The obtained small external quantum efficiency [Fig. S8(b)] primarily results from a weak collection of hot electrons in graphene. Additionally, the region of light-matter interaction (contributing to photocurrent) mainly occurs upon graphene on the top of the waveguide; therefore, reducing sheet resistance of MoTe₂ can optimize external quantum efficiency.²⁸ For instance, another graphene/MoTe₂ heterojunction device in Fig. S9(d) (MoTe₂ thickness: 33 nm) with smaller sheet resistance and larger dark current shows a larger responsivity of 0.64 mA \cdot W⁻¹ (-1 V) at 1547.74 nm (resonance wavelength).

We also measured noise currents under different conditions. The current noise is related to driven frequency in Fig. 4(d), which would be determined by the Hooge's empirical relationship ($S_i = A \cdot i^2 / f^\beta$),⁴⁵ where i , f , and A are the channel current, driven frequency, and noise amplitude, respectively. Under optical illumination, a larger noise (pink line) can be observed, accompanied by the increasing channel current. Intriguingly, a smaller frequency reaching the white noise floor seems to be obtained under illumination, indicating the different fluctuation processes of charge carrier number and mobility.⁴⁶ Current noise induced by shot noise, which is about 100 times larger than thermal noise, is the primary origin of white noise. Under a reverse bias voltage, both a smaller current noise and noise-equivalent power (NEP) can be realized, resulting from the smaller dark current and higher efficiency for photon-to-electron transition.

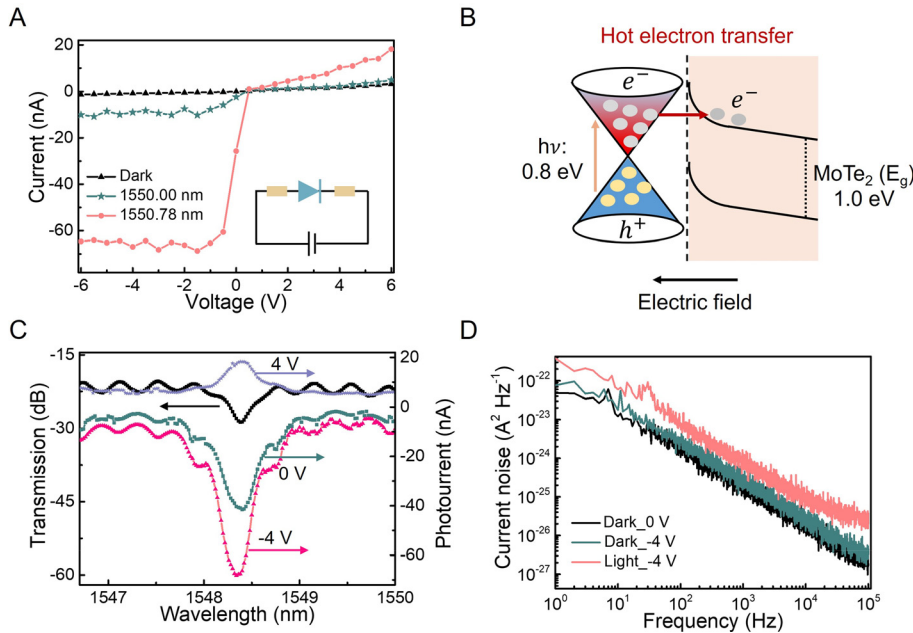


FIG. 4. Photon-to-electron transition performance. (a) IV curves of an MRR-integrated graphene/MoTe₂ heterojunction photodetector in the dark and under illumination at resonance (1550.78 nm) and non-resonance (1550.00 nm) wavelengths, input optical power is 0.14 mW. The illustration is the equivalent circuit of the graphene/MoTe₂ heterojunction device, consisting of two parts of sheet resistance (graphene and MoTe₂) and a diode. (b) Energy band of graphene/MoTe₂ heterojunction photodetector at 0 V and under the reverse bias voltage under illumination of 1550 nm. (c) Optoelectronic response at different wavelengths of the MRR-integrated graphene/MoTe₂ heterojunction photodetector driven under bias voltages, and the transmission spectrum at 0 V. (d) Noise power spectra density of a graphene/MoTe₂ heterojunction device under different conditions, input optical power is 0.14 mW (pink line).

The proposed graphene/MoTe₂ heterojunction devices have a dual function as both optical modulators and photodetectors. This innovative design not only reduces the fabrication complexity and decreases the insertion loss but also offers expanded possibilities for integrated photonic circuit applications. Simultaneously, this graphene/MoTe₂ heterojunction device with multiple functionalities demonstrates obvious advantages in performance compared with those reported waveguide-integrated photonic devices based on 2DMs, and the detailed comparison is shown in Table S1. Among these 2DMs-based integrated photonic devices,^{20,35,39,47–49} graphene/MoTe₂ heterojunction photonic devices show superiorities in MD, footprint, and bandwidth for an optical modulator and self-driven photo-response for a photodetector. In further, optimizing contact resistance between 2DMs/metal contact, reducing sheet resistance of MoTe₂, and shortening the channel length with a vertical structure can improve optoelectronic performance, such as a faster dynamic response and a higher responsivity.

III. CONCLUSION

In summary, we demonstrated the graphene/MoTe₂ heterojunction integrated with MRRs to realize dual-functional photonic applications in optical modulators and photodetectors. In such a device, monolayer graphene not only serves as a photoactive material to realize photon-to-electron transition for photodetection but also works as a refractive index-tunable material by accumulating carriers to change the MRR coupled condition for optical modulation. The MRR-integrated heterojunction devices can realize a modulation depth of ~26.7 dB, a $f_{3\text{-dB}}$ of 7.0 GHz, and a self-driven, wavelength-sensitive optoelectronic response at the C band. Such a van der Waals heterojunction can integrate with arbitrary optical platforms, opening wide possibilities in emerging photonic applications such as optical neural networks and nonlinear optics and expanding the freedom for miniaturized photonic circuits.

IV. METHODS

A. Device fabrication

The integrated photonic devices were fabricated with standard 220-nm-SOI multi-project wafer (MPW) processes in IMECAS. The top surface of the devices is filled back by SiO₂, and then it is polished by the chemical and mechanical process to achieve a flat surface. We then transfer CVD-grown monolayer graphene onto the photonic devices by a wet transfer process with a sacrificial layer (PMMA). As for the processes of wet transfer, PMMA was first coated onto graphene surface with baking at 120 °C for 10 min and then copper foil was removed by ferric chloride solution. After removing PMMA by acetone, UV lithography was applied to pattern the device to protect the desired area, and the excess graphene region was removed by plasma etch technology. Next, the area of metal contacts (Ti/Au, 5/100 nm) was patterned by UV lithography, and the metal film was deposited by the electron-beam evaporation (ULvac vacuum technology (Suzhou) Co., Ltd, Ei-5Z) and then obtained the clean metal contacts after a standard lift-off process. Eventually, multilayer MoTe₂ samples were exfoliated from bulk crystal (purchased from Taizhou SUNANO New Energy CO., Ltd.) by Scotch tape, aligned, and transferred onto the top of graphene with the assistance of polydimethylsiloxane to form a heterojunction.

B. Device characterizations

Raman spectra (WITec, Alpha300R) were used to evaluate the quality of graphene and MoTe₂. Thickness and surface potential of graphene/MoTe₂ heterojunction were conducted by atomic force microscope (Oxford Instruments, Cypher ES), and the morphology of the heterojunction device was characterized by SEM (Hitachi, Regulus 8230). Characterizations of the static optoelectronic response for photodetectors were realized by a semiconductor analyzer (PDA, FS-Pro) and excited by a tunable semiconductor laser (Santec Corporation,

TSL-550) with wavelengths ranging from 1260 to 1620 nm. Characterizations of spectra transmission were finished by a tunable semiconductor laser and driven by a source meter (Keithley 2450). The setups of $f_{3\text{-dB}}$ bandwidth characterization for a modulator are shown in Fig. S10, in which the RF signal was generated and collected by a vector network analyzer (Anritsu, MS4647B). A commercial photodetector was used to transform the optical signal into an electrical signal, working as the input for the vector network analyzer. The setups of eye diagram characterization for a modulator are shown in Fig. S12, where the fabricated modulator was driven by a signal quality analyzer-R (Anritsu, MP 1900A), which can provide a $2^{31}-1$ pseudo-random binary sequence. The modulated optical signal was amplified by Erbium-doped fiber amplifier (Amonics, AEDFA-PA-35-B-FA), and then was received by a sampling oscilloscope with an optical module (Anritsu, MP2110A).

SUPPLEMENTARY MATERIAL

See the [supplementary material](#) for additional information and figures.

ACKNOWLEDGMENTS

The authors thank Westlake Center for Micro/Nano Fabrication and Instrumentation and Service Center for Physical Sciences and Molecular Sciences at Westlake University for the facility support, ZJU Micro-Nano Fabrication Center at Zhejiang University. We thank Dr. Zhong Chen for Raman measurement and Westlake HPC Center for technical assistance. The research was partially supported by the National Natural Science Foundation of China (Grant Numbers 12104375, 62175202, 61975179, and 91950204), Zhejiang Provincial Natural Science Foundation of China (No. LD22F040002), Leading Innovative and Entrepreneur Team Introduction Program of Zhejiang (No. 2020R01005), Key Project of Westlake Institute for Optoelectronics (No. 2023GD003/110500Y0022303), and Special Support Plan for Photoelectric Chips Research at Westlake University (No. 10300000H062401).

AUTHOR DECLARATIONS

Conflict of Interest

The authors have no conflicts to disclose.

Author Contributions

Jianghong Wu: Conceptualization (lead); Data curation (lead); Formal analysis (lead); Investigation (lead); Methodology (lead); Software (equal); Validation (lead); Visualization (equal); Writing – original draft (lead); Writing – review & editing (lead). **Jialing Jian:** Data curation (equal); Investigation (equal); Methodology (equal); Software (equal); Validation (equal). **Boshu Sun:** Investigation (equal); Methodology (equal); Writing – original draft (equal). **Yuting Ye:** Investigation (equal); Methodology (equal); Validation (equal). **Hui Ma:** Methodology (equal); Project administration (equal); Visualization (equal). **Bo Tang:** Methodology (equal). **Qingyan Deng:** Investigation (equal); Software (equal). **Renjie Tang:** Investigation (equal). **Junying Li:** Methodology (equal). **Chunlei Sun:** Investigation (equal). **Hongtao Lin:** Funding acquisition (equal); Project administration (equal); Supervision (equal); Writing – review & editing (equal). **Lan Li:** Conceptualization (lead); Data curation (lead); Formal analysis

(lead); Funding acquisition (lead); Investigation (lead); Project administration (lead); Resources (lead); Supervision (lead); Writing – original draft (lead); Writing – review & editing (lead).

DATA AVAILABILITY

The data that support the findings of this study are available within the article and its [supplementary material](#).

REFERENCES

- Y. C. Wang, K. D. Jöns, and Z. P. Sun, “Integrated photon-pair sources with nonlinear optics,” *Appl. Phys. Rev.* **8**, 011314 (2021).
- M. Thomaschewski and S. I. Bozhevolnyi, “Pockels modulation in integrated nanophotonics,” *Appl. Phys. Rev.* **9**, 021311 (2022).
- G. Liang, H. Huang, A. Mohanty, M. C. Shin, X. Ji, M. J. Carter, S. Shrestha, M. Lipson, and N. Yu, “Robust, efficient, micrometre-scale phase modulators at visible wavelengths,” *Nat. Photonics* **15**, 908–913 (2021).
- L. Li, H. T. Lin, S. T. Qiao, Y. Zou, S. Danto, K. Richardson, J. D. Musgraves, N. S. Lu, and J. J. Hu, “Integrated flexible chalcogenide glass photonic devices,” *Nat. Photonics* **8**, 643–649 (2014).
- Y. A. Vlasov, “Silicon CMOS-integrated nano-photonics for computer and data communications beyond 100G,” *IEEE Commun. Mag.* **50**, s67–s72 (2012).
- R. Tang, C. Sun, K. Bao, Z. Chen, Z. Ju, M. Wei, Y. Wu, J. Wu, K. Xu, H. Lin, and L. Li, “High-resolution 2D quasi-distributed optical sensing with on-chip multiplexed FSR-free nanobeam cavity array,” *Laser Photonics Rev.* **18**, 2300828 (2024).
- P. F. Xu and Z. P. Zhou, “Silicon-based optoelectronics for general-purpose matrix computation: A review,” *Adv. Photonics* **4**, 044001 (2022).
- W. Bogaerts, D. Pérez, J. Capmany, D. A. B. Miller, J. Poon, D. Englund, F. Morichetti, and A. Melloni, “Programmable photonic circuits,” *Nature* **586**, 207–216 (2020).
- Y. Huang, W. Wang, L. Qiao, X. Hu, and T. Chu, “Programmable low-threshold optical nonlinear activation functions for photonic neural networks,” *Opt. Lett.* **47**, 1810–1813 (2022).
- C. Pappas, S. Kovalios, M. Moralis-Pegios, A. Tsakyridis, G. Giamougiannis, M. Kirtas, J. Van Kerrebrouck, G. Coudyzer, X. Yin, N. Passalis, A. Tefas, and N. Pleros, “Programmable tanh-, ELU-, sigmoid-, and sin-based nonlinear activation functions for neuromorphic photonics,” *IEEE J. Sel. Top. Quantum Electron.* **29**, 6101210 (2023).
- B. J. Shastri, A. N. Tait, T. Ferreira de Lima, W. H. Pernice, H. Bhaskaran, C. D. Wright, and P. R. Prucnal, “Photonics for artificial intelligence and neuromorphic computing,” *Nat. Photonics* **15**, 102–114 (2021).
- G. H. Ahn, A. D. White, H. Kim, N. Higashitarumizu, F. M. Mayor, J. F. Herrmann, W. Jiang, K. K. Multani, A. H. Safavi-Naeini, and A. Javey, “Platform-agnostic waveguide integration of high-speed photodetectors with evaporated tellurium thin films,” *Optica* **10**, 349–355 (2023).
- J. Wu, Y. Ye, J. Jian, X. Yao, J. Li, B. Tang, H. Ma, M. Wei, W. Li, H. Lin, and L. Li, “Reversible thermally driven phase change of layered In_2Se_3 for integrated photonics,” *Nano Lett.* **23**, 6440–6448 (2023).
- X.-J. Liu, Y. Yu, D. Liu, Q.-L. Cui, X. Qi, Y. Chen, G. Qu, L. Song, G.-P. Guo, G.-C. Guo, X. Sun, and X.-F. Ren, “Coupling of photon emitters in monolayer WS_2 with a photonic waveguide based on bound states in the continuum,” *Nano Lett.* **23**, 3209–3216 (2023).
- X. T. Gan, D. Englund, D. Van Thourhout, and J. L. Zhao, “2D materials-enabled optical modulators: From visible to terahertz spectral range,” *Appl. Phys. Rev.* **9**, 021302 (2022).
- Y. Hu, M. Pantouvaki, J. Van Campenhout, S. Brems, I. Asselberghs, C. Huyghebaert, P. Absil, and D. Van Thourhout, “Broadband 10 Gb/s operation of graphene electro-absorption modulator on silicon,” *Laser Photonics Rev.* **10**, 307–316 (2016).
- Y. Gao, R.-J. Shiue, X. Gan, L. Li, C. Peng, I. Meric, L. Wang, A. Szep, D. Walker, Jr., J. Hone, and D. Englund, “High-speed electro-optic modulator integrated with graphene-boron nitride heterostructure and photonic crystal nanocavity,” *Nano Lett.* **15**, 2001–2005 (2015).

- ¹⁸L. Liu, A. V. Krasavin, J. Li, L. Li, L. Yang, X. Guo, D. Dai, A. V. Zayats, L. Tong, and P. Wang, "Waveguide-integrated light-emitting metal-insulator-graphene tunnel junctions," *Nano Lett.* **23**, 3731–3738 (2023).
- ¹⁹H. Lin, Y. Song, Y. Huang, D. Kita, S. Deckoff-Jones, K. Wang, L. Li, J. Li, H. Zheng, and Z. Luo, "Chalcogenide glass-on-graphene photonics," *Nat. Photonics* **11**, 798–805 (2017).
- ²⁰N. Youngblood, Y. Anugrah, R. Ma, S. J. Koester, and M. Li, "Multifunctional graphene optical modulator and photodetector integrated on silicon waveguides," *Nano Lett.* **14**, 2741–2746 (2014).
- ²¹S. Schuler, D. Schall, D. Neumaier, L. Dobusch, O. Bethge, B. Schwarz, M. Krall, and T. Mueller, "Controlled generation of a p-n junction in a waveguide integrated graphene photodetector," *Nano Lett.* **16**, 7107–7112 (2016).
- ²²Y. Ding, X. Guan, X. Zhu, H. Hu, S. I. Bozhevolnyi, L. K. Oxenlowe, K. J. Jin, N. A. Mortensen, and S. Xiao, "Efficient electro-optic modulation in low-loss graphene-plasmonic slot waveguides," *Nanoscale* **9**, 15576–15581 (2017).
- ²³L. Colombo, R. M. Wallace, and R. S. Ruoff, "Graphene growth and device integration," *Proc. IEEE* **101**, 1536–1556 (2013).
- ²⁴I. Datta, A. Gil-Molina, S. H. Chae, V. Zhou, J. Hone, and M. Lipson, "2D material platform for overcoming the amplitude-phase tradeoff in ring resonators," *Optica* **11**, 48–57 (2024).
- ²⁵C. T. Phare, Y.-H. Daniel Lee, J. Cardenas, and M. Lipson, "Graphene electro-optic modulator with 30 GHz bandwidth," *Nat. Photonics* **9**, 511–514 (2015).
- ²⁶G. T. Reed, G. Z. Mashanovich, F. Y. Gardes, M. Nedeljkovic, Y. Hu, D. J. Thomson, K. Li, P. R. Wilson, S.-W. Chen, and S. S. Hsu, "Recent breakthroughs in carrier depletion based silicon optical modulators," *Nanophotonics* **3**, 229–245 (2014).
- ²⁷H. Wang, H. Dalir, C. Patil, and V. J. Sorger, *Waveguide Integrated MoTe₂ Photodetector with High Speed and Energy Efficient* (IEEE, 2022).
- ²⁸N. Flöry, P. Ma, Y. Salamin, A. Emboras, T. Taniguchi, K. Watanabe, J. Leuthold, and L. Novotny, "Waveguide-integrated van der Waals heterostructure photodetector at telecom wavelengths with high speed and high responsivity," *Nat. Nanotechnol.* **15**, 118–124 (2020).
- ²⁹Y. Liu, J. Guo, E. Zhu, L. Liao, S.-J. Lee, M. Ding, I. Shakir, V. Gambin, Y. Huang, and X. Duan, "Approaching the Schottky-Mott limit in van der Waals metal-semiconductor junctions," *Nature* **557**, 696–700 (2018).
- ³⁰J. B. Wu, M. L. Lin, X. Cong, H. N. Liu, and P. H. Tan, "Raman spectroscopy of graphene-based materials and its applications in related devices," *Chem. Soc. Rev.* **47**, 1822–1873 (2018).
- ³¹A. C. Ferrari and D. M. Basko, "Raman spectroscopy as a versatile tool for studying the properties of graphene," *Nat. Nanotechnol.* **8**, 235–246 (2013).
- ³²S. Ryu, L. Liu, S. Berciaud, Y.-J. Yu, H. Liu, P. Kim, G. W. Flynn, and L. E. Brus, "Atmospheric oxygen binding and hole doping in deformed graphene on a SiO₂ substrate," *Nano Lett.* **10**, 4944–4951 (2010).
- ³³S. J. Koester and M. Li, "Waveguide-coupled graphene optoelectronics," *IEEE J. Sel. Top. Quantum Electron.* **20**, 84–94 (2013).
- ³⁴M. Liu, X. Yin, E. Ulin-Avila, B. Geng, T. Zentgraf, L. Ju, F. Wang, and X. Zhang, "A graphene-based broadband optical modulator," *Nature* **474**, 64–67 (2011).
- ³⁵V. Soriano, M. Midrio, G. Contestabile, I. Asselberghs, J. Van Campenhout, C. Huyghebaert, I. Goykhman, A. Ott, A. Ferrari, and M. Romagnoli, "Graphene-silicon phase modulators with gigahertz bandwidth," *Nat. Photonics* **12**, 40–44 (2018).
- ³⁶A. Majumdar, J. Kim, J. Vuckovic, and F. Wang, "Electrical control of silicon photonic crystal cavity by graphene," *Nano Lett.* **13**, 515–518 (2013).
- ³⁷A. Vakil and N. Engheta, "Transformation optics using graphene," *Science* **332**, 1291–1294 (2011).
- ³⁸X. Hu, Y. Zhang, D. Chen, X. Xiao, and S. Yu, "Design and modeling of high efficiency graphene intensity/phase modulator based on ultra-thin silicon strip waveguide," *J. Lightwave Technol.* **37**, 2284–2292 (2019).
- ³⁹I. Datta, S. H. Chae, G. R. Bhatt, M. A. Tadayon, B. Li, Y. Yu, C. Park, J. Park, L. Cao, and D. Basov, "Low-loss composite photonic platform based on 2D semiconductor monolayers," *Nat. Photonics* **14**, 256–262 (2020).
- ⁴⁰S. Y. Siew, B. Li, F. Gao, H. Y. Zheng, W. Zhang, P. Guo, S. W. Xie, A. Song, B. Dong, L. W. Luo, C. Li, X. Luo, and G. Q. Lo, "Review of silicon photonics technology and platform development," *J. Lightwave Technol.* **39**, 4374–4389 (2021).
- ⁴¹M. Liu, X. Yin, and X. Zhang, "Double-layer graphene optical modulator," *Nano Lett.* **12**, 1482–1485 (2012).
- ⁴²C. Qiu, W. Gao, R. Vajtai, P. M. Ajayan, J. Kono, and Q. Xu, "Efficient modulation of 1.55 μm radiation with gated graphene on a silicon microring resonator," *Nano Lett.* **14**, 6811–6815 (2014).
- ⁴³R. Maiti, C. Patil, M. A. S. R. Saadi, T. Xie, J. G. Azadani, B. Uluutku, R. Amin, A. F. Briggs, M. Miscuglio, D. Van Thourhout, S. D. Solares, T. Low, R. Agarwal, S. R. Bank, and V. J. Sorger, "Strain-engineered high-responsivity MoTe₂ photodetector for silicon photonic integrated circuits," *Nat. Photonics* **14**, 578–584 (2020).
- ⁴⁴K. J. Tielrooij, L. Piatkowski, M. Massicotte, A. Woessner, Q. Ma, Y. Lee, K. S. Myhro, C. N. Lau, P. Jarillo-Herrero, N. F. van Hulst, and F. H. L. Koppens, "Generation of photovoltage in graphene on a femtosecond timescale through efficient carrier heating," *Nat. Nanotechnol.* **10**, 437–443 (2015).
- ⁴⁵F. N. Hooge, T. G. M. Kleinpenning, and L. K. J. Vandamme, "Experimental studies on 1/f noise," *Rep. Prog. Phys.* **44**, 479 (1981).
- ⁴⁶A. A. Balandin, "Low-frequency 1/f noise in graphene devices," *Nat. Nanotechnol.* **8**, 549–555 (2013).
- ⁴⁷H. Chen, Z. Zhao, Z. Zhang, G. Wang, J. Li, Z. Shang, M. Zhang, K. Guo, J. Yang, and P. Yan, "Heterogeneous integrated phase modulator based on two-dimensional layered materials," *Photonics Res.* **10**, 1401–1407 (2022).
- ⁴⁸E. Heidari, H. Dalir, F. M. Koushyar, B. M. Nouri, C. Patil, M. Miscuglio, D. Akinwande, and V. J. Sorger, "Integrated ultra-high-performance graphene optical modulator," *Nanophotonics* **11**, 4011–4016 (2022).
- ⁴⁹C. Wu, S. Brems, D. Yudistira, D. Cott, A. Milenin, K. Vandersmissen, A. Maestre, A. Centeno, A. Zurutuza, J. Van Campenhout, C. Huyghebaert, D. Van Thourhout, and M. Pantouvaki, "Wafer-scale integration of single layer graphene electro-absorption modulators in a 300 mm CMOS pilot line," *Laser Photonics Rev.* **17**, 2200789 (2023).